Acta Materialia 221 (2021) 117423

Contents lists available at ScienceDirect

Acta Materialia

journal homepage: www.elsevier.com/locate/actamat

Full Length Article

Strain relaxation and dislocation annihilation in compositionally graded α-$(Al_xGa_{1-x})_2O_3$ layer for high voltage α-Ga_2O_3 power devices

Byungsoo Kim[a], Duyoung Yang[a], Woonbae Sohn[a], Seungmin Lee[a], Hwan-Hee-Chan Choi[c], Taehoon Jang[c], Euijoon Yoon[a], Yongjo Park[b,*], Ho Won Jang[a,b,*]

[a] Department of Materials Science and Engineering, Research Institute of Advanced Materials, Seoul National University, Seoul 08826 Republic of Korea
[b] Advanced Institute of Convergence Technology, Seoul National University, Suwon 16229 Republic of Korea
[c] Sigetronics Inc, Jeonbuk 55314 Republic of Korea

ARTICLE INFO

Article history:
Received 24 June 2021
Revised 14 October 2021
Accepted 17 October 2021
Available online 21 October 2021

Keywords:
Gallium oxide
Epitaxial growth
Single crystalline
Lattice strain
Dislocation annihilation
Schottky diode

ABSTRACT

α-Ga_2O_3 of the corundum structure and the large bandgap of 5.3 eV has attracted great interest because it can be grown on a sapphire (α-Al_2O_3) substrate with the same crystal structure. However, the lattice mismatch (4.3%) and the different thermal expansion coefficients between α-Ga_2O_3 and the sapphire substrate induce crystalline defects and thermal strain, leading to a high density of threading dislocations and degraded electrical properties of the α-Ga_2O_3 films grown directly on the substrate. Herein, to circumvents these issues, compositionally graded α-$(Al_xGa_{1-x})_2O_3$ layers are adopted to reduce threading dislocations for a high quality of epitaxial α-Ga_2O_3 films. The evolution of strain relaxation and the inclination of threading dislocations in graded α-$(Al_xGa_{1-x})_2O_3$ layers are confirmed by reciprocal space mapping (RSM) and transmission electron microscopy (TEM). Through RSM and TEM studies, we confirmed that compressive strain enhances the inclination of dislocations, and therefore, the dislocations merge and annihilate in the graded α-$(Al_xGa_{1-x})_2O_3$ layers. Moreover, owing to dislocations annihilation in the graded α-$(Al_xGa_{1-x})_2O_3$ layers, the calculated density of threading dislocations in α-Ga_2O_3 films with a graded α-$(Al_xGa_{1-x})_2O_3$ layer is reduced by 64.9% compared with that of α-Ga_2O_3 films deposited directly grown on a bare sapphire substrate. Furthermore, a fabricated lateral-structure Schottky diodes reveals enhanced breakdown voltages and forward current density due to the improved crystalline quality using the graded α-$(Al_xGa_{1-x})_2O_3$ layer. This study provides an attractive approach for obtaining high-quality epitaxial α-Ga_2O_3 thin films for high voltage power devices.

1. Introduction

Power electronics are indispensable for efficient energy conversion in electrical energy applications such as electric vehicles, electric transmission, and wireless communication systems [1,2]. Due to the limited options for semiconductor switches that operate above 10 kV, current Si-based power electronics use a transformer to step down the high voltage and then step it back up to the desired voltage, which results in a large energy conversion loss [3]. Recently, ultrawide bandgap (UWBG) semiconductors including Ga_2O_3, silicon carbide (SiC), diamond, and GaN have been suggested as good candidates to replace Si-based power electronics for high voltage applications [4–6,49,50].

Among wide-bandgap materials, gallium oxide (Ga_2O_3) has gained considerable attention due to its stable physical and chemical properties. Its interesting properties include a wide bandgap of 5.0–5.3 eV, [7] a high breakdown voltage of 8 MV/cm [8], and UV transparency [9], which have caused it to be proposed for high power applications and solar-blind photodetectors [10,11]. Ga_2O_3 has five known polymorphs (α, β, ε, γ, and δ) [12–16] and among them β-Ga_2O_3 has been widely studied because it is the most thermodynamically stable phase and the availability of high-quality β-Ga_2O_3 bulk substrates obtained by various growth methods such as edge-defined film-fed growth (EFG) [17] and the Czochralski method [18]. However, the bottleneck for β-Ga_2O_3 is the higher cost of a single crystal substrate wafer than a sapphire substrate. The corundum structure α-Ga_2O_3, a thermodynamically metastable phase of Ga_2O_3, has a large bandgap of 5.3 eV, which can enhance the performance of power devices [19]. In addition, α-Ga_2O_3 belongs to the same corundum structure as α-Al_2O_3 (sapphire), and thus α-Ga_2O_3 can be obtained from heteroepitaxial growth by using a sapphire substrate. Furthermore, it is possible to make an alloy with other corundum structures of α-Al_2O_3 and α-In_2O_3 for bandgap engineering and

* Corresponding authors at: Advanced Institute of Convergence Technology, Seoul National University, Suwon 16229 Republic of Korea.
E-mail addresses: yp0520@snu.ac.kr (Y. Park), hwjang@snu.ac.kr (H.W. Jang).

https://doi.org/10.1016/j.actamat.2021.117423
1359-6454/

grow heteroepitaxial p-type corundum structured α-Ir_2O_3 on α-Ga_2O_3 with an in-plane lattice mismatch of less than 0.3% [20]. For heteroepitaxial α-Ga_2O_3 on a sapphire substrate, mist chemical vapor deposition (Mist-CVD) [21,22] and hydride vapor phase epitaxy have been used most frequently [23,24]. However, one of the problems of the heteroepitaxial growth of α-Ga_2O_3 on a sapphire substrate is the large lattice between α-Ga_2O_3 and α-Al_2O_3 ($\Delta a/a \sim 4.5\%$, $\Delta c/c \sim 3.3\%$) [25,26], which leads to dislocations such as misfit dislocations (MDs) and threading dislocations (TDs). The threading dislocations negatively affect the electrical properties of the hetero-epitaxial layer in that it induces a conduction channel leakage path and reduces carrier mobility [27]. To circumvent these issues, a metamorphic buffer layer for minimizing dislocations caused by lattice mismatch is needed. The ternary alloy α-$(Al_xGa_{1-x})_2O_3$, with an intermediate lattice constant between α-Ga_2O_3 and α-Al_2O_3, is an adequate candidate for reducing lattice mismatch [28]. Previously, Jinno et al. have reported that by applying a complicated α-$(Al_xGa_{1-x})_2O_3$ superlattice with $x = 0.1$ and $x = 0.9$, the total threading dislocation density (TDD) of α-Ga_2O_3 was decreased from 7×10^{10} cm^{-2} to 9×10^8 cm^{-2} [29]. However, the strain distribution in strain distribution in α-$(Al_xGa_{1-x})_2O_3$ buffer was not investigated in detail. Recently, G.T. Dang et al. have reported a conductive n-type α-Ga_2O_3 grown on various α-$(Al_xGa_{1-x})_2O_3$ buffer configurations and fabricated PtO_x and AgO_x Schottky diodes [30]. However, the evolution of TDs according to strain relaxation in α-$(Al_xGa_{1-x})_2O_3$ buffer has not been clarified, which is essential for the improvement of α-Ga_2O_3 based high voltage power devices.

In this study, we demonstrate high-quality α-Ga_2O_3 epitaxial films by adopting a graded α-$(Al_xGa_{1-x})_2O_3$ buffer layer with x = 0.11–0.87, which results in an observable reduction of TD density compared with directly grown on the sapphire substrate. We found that the evolution of strain relaxation in an α-$(Al_xGa_{1-x})_2O_3$ buffer layer affected the inclination of TDs, resulting in the annihilation of TDs. As a result, the total threading dislocation density (TDD) of the α-Ga_2O_3 films grown on graded α-$(Al_xGa_{1-x})_2O_3$ layer was observably reduced to a low value 7.3×10^9 cm^{-2}, which is 64.9% less than that of the α-Ga_2O_3 films on directly grown on the sapphire substrate. Moreover, the corresponding Schottky diodes reveals enhanced breakdown voltage and conductivity due to the reduction of TDs by using a graded α-$(Al_xGa_{1-x})_2O_3$ layer. This study can provide an attractive approach for obtaining high-quality epitaxial α-Ga_2O_3 thin films for high voltage power devices.

2. Experimental

2.1. Epitaxial growth

Epitaxial α-Ga_2O_3/α-$(Al_xGa_{1-x})_2O_3$ films were grown on a sapphire substrate by Mist-CVD, as described in detail in the Supplementary Materials, Fig. S1. Gallium chloride ($GaCl_3$ Sigma Aldrich, 99.99%) and aluminum acetylacetonate ($Al(C_5H_8O_3)_3$ Sigma Aldrich, 99.99%) were diluted in slightly acidified water (HCl, Sam-Chun, 36.5%) as precursors for Ga and Al at a concentration of 0.05 and 0.1 M, respectively. To control Al composition in the α-$(Al_xGa_{1-x})_2O_3$ layer, the gas flow rate of [Al]/[Ga + Al] was varied between 2.35 and 90%. Gallium acetylacetonate ($Ga(C_5H_8O_3)_3$, Sigma Aldrich, 99.99%) with tin chloride ($SnCl_3$ Sigma Aldrich, 99.99%)) as an n-type dopant was mixed in slightly acidic water at a [Sn]/[Ga] mixing ratio of 0.05%. Half of the 2-inch c-sapphire wafers were loaded into a chamber with nitrogen (N_2) as the carrier gas. 0.35 μm-thick α-$(Al_xGa_{1-x})_2O_3$ layers were grown at 500°C with different Al compositions and named samples A, B, and C. Subsequently, 2.0 μm-thick α-Ga_2O_3 epitaxial films were grown on the α-$(Al_xGa_{1-x})_2O_3$ layers at 500°C, as shown in Fig. 1a. The in-plane lattice mismatch (%) based on the varying Al contents was examined, as shown in Fig. 1b. To investigate the effect of the electrical properties on α-Ga_2O_3 films with the graded α-$(Al_xGa_{1-x})_2O_3$ layer, 2 μm-thick Sn-doped n-type α-Ga_2O_3 layers were grown followed by a 0.35 μm-thick graded α-$(Al_xGa_{1-x})_2O_3$ layer, as shown in Fig. 7a.

2.2. Fabrication of lateral Schottky diode

The lateral-Schottky diode was fabricated by using a photolithographic technique. Al_2O_3 (15 nm) passivation layer was deposited by atomic layer deposition on photoresist-patterned samples. Ti /Au (20/50 nm) ohmic contact metal was deposited by electron-beam evaporation. Subsequently, after the lift-off of the metal on the photoresist, the ohmic metal was annealed using a rapid thermal annealing (RTA) system at 500 °C for 1 min under ambient N_2. Then, the Pt (20 nm) Schottky contact metal was surrounded by the Ti/Au ohmic contact metal. The gap spacing between the ohmic metal and Schottky metal was 50 μm.

2.3. Characterization

Surface morphology images were acquired with a field emission-scanning electron microscope (FE-SEM, Merin-Compact). The crystal phase of the epitaxial α-Ga_2O_3/α-$(Al_xGa_{1-x})_2O_3$ grown on the c-sapphire substrate was analyzed with an X-ray diffractometer (XRD, Bruker Co., D8-Advance). Crystal quality and reciprocal space mapping (RSM) were conducted by a PANalytical X'pert Pro triple-axis diffractometer equipped with a 4-bounce Ge (220) hybrid monochromator. To observe the lattice distortion at the interlayer interface, cross-section transmission electron microscopy (TEM) images of the α-Ga_2O_3/α-$(Al_xGa_{1-x})_2O_3$ on the sapphire substrate were obtained with a JEOL JEM-2100F at an acceleration voltage of 200 kV. The threading dislocation density (TDD) was calculated from the mosaic tilt and twist angles according to the inclination X-ray angle of the high-resolution XRD. The free electron concentration (n) and Hall mobility (μ) in 2.0 μm-thick n^- α-Ga_2O_3 on sapphire were measured by Hall-effect measurement. In addition, the current-voltage (J-V) characteristics of the lateral Schottky barrier diodes were measured with a STI 5000C semiconductor parameter analyzer.

3. Results and discussion

The crystal phase of the epitaxial α-Ga_2O_3/α-$(Al_xGa_{1-x})_2O_3$ grown on the sapphire substrate was measured with XRD. Fig. 2a shows the profiles of the XRD $2\theta/\omega$ scanning spectra for α-$(Al_xGa_{1-x})_2O_3$ thin films with different amounts of Al content grown on sapphire substrates. The Al content in the α-$(Al_xGa_{1-x})_2O_3$ was systematically controlled by the [Ga] and [Al] carrier gas flow rate. The peak of the epitaxially grown α-$(Al_xGa_{1-x})_2O_3$ thin films systematically shifted from α-Ga_2O_3 0006 at $2\theta = 40.625°$ (PDF#00-006-0503) toward α-Al_2O_3 0006 at $2\theta = 41.67°$ (PDF#00-046-1212) as the amount of Al increased. For the determination of the Al content in the α-$(Al_xGa_{1-x})_2O_3$ thin films, we assumed that the epitaxial α-$(Al_xGa_{1-x})_2O_3$ thin films were fully relaxed, and the lattice parameter of the ternary alloy varied linearly with the chemical composition. The relevant parameters of fully relaxed α-$(Al_xGa_{1-x})_2O_3$ layers could be calculated using Vegard's law with the XRD peak positions [31]. From Vegard's law, we confirmed that the Al fraction of the epitaxial α-$(Al_xGa_{1-x})_2O_3$ layer was $x = 6$–89%. It is worth noting that the alloy of β-$(Al_xGa_{1-x})_2O_3$ has a limitation with high Al incorporation due to the different ground state of the crystal structure of monoclinic β-Ga_2O_3 and corundum α-Al_2O_3 [32]. On the other hand, the ternary α-$(Al_xGa_{1-x})_2O_3$ has the same crystal structure as α-Al_2O_3 and α-Ga_2O_3, and it can be grown on a sapphire substrate

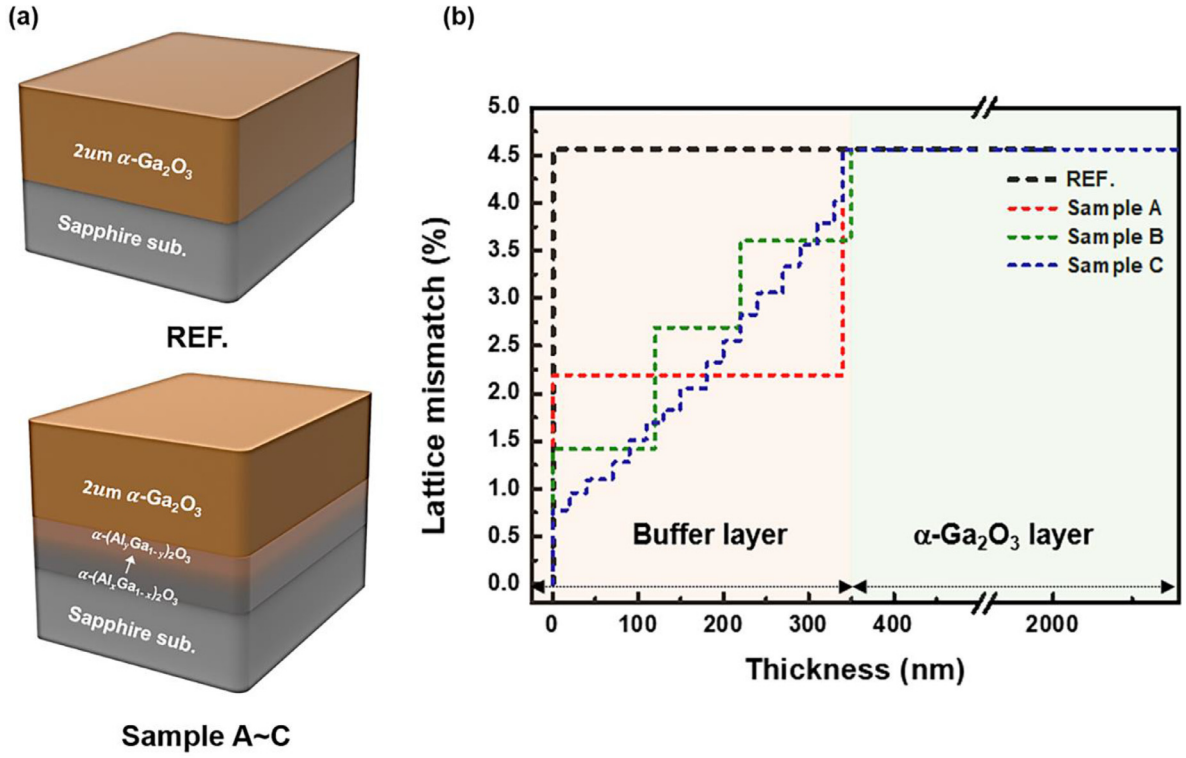

Fig. 1. (a) Schematic of α-Ga_2O_3/sapphire substrate and α-Ga_2O_3/α-$(Al_xGa_{1-x})_2O_3$/sapphire substrate. (b) In-plane lattice mismatch as a function of thickness for α-$(Al_xGa_{1-x})_2O_3$ grown on the sapphire substrate.

over the entire Al composition range of x without phase separation, as shown in Fig. 2a. However, as the Al content increased, the XRD intensity of α-$(Al_xGa_{1-x})_2O_3$ thin films decreased. The main reason for the decrease in XRD peak intensity is degradation of the crystallinity in α-$(Al_xGa_{1-x})_2O_3$ thin films as Al composition increase. Fig. 2b shows the surface morphologies of α-$(Al_xGa_{1-x})_2O_3$ with different amounts of Al, as characterized by FE-SEM and AFM. As the amount of Al increases, the surface roughness increased from 1.11 to 1.32 nm. For low Al content, a longer diffusion length of the Ga adatom than that of Al promoted lateral growth, which increased the grain size, induced the coalescence of the neighboring island, and facilitated two-dimensional (2D) growth with a low density of islands. In contrast, when the Al content in α-$(Al_xGa_{1-x})_2O_3$ was high, the Al adatoms have weaker migration than Ga adatoms on the substrate surface, which resulted in a high density of islands and facilitated three-dimensional (3D) growth with a high density of islands [33,34]. In general, for the high density of islands with 3D growth mode, two adjacent islands coalesce to minimize the sum of elastic energy and surface energy, leading to tensile stress [35] This resulted in undesirable tensile stress and generation of dislocation in α-$(Al_xGa_{1-x})_2O_3$ thin films. Thus, the island density according to the Al content affected the generation of dislocation at the coalescence boundary, resulting in the crystallinity degradation in α-$(Al_xGa_{1-x})_2O_3$ thin films.

Fig. 2c shows the plot of the $2\theta/\omega$ scan profiles for α-Ga_2O_3/α-$(Al_xGa_{1-x})_2O_3$ grown on sapphire in the samples A, B, and C. We can observe the peaks of α-Ga_2O_3 0006 at $2\theta = 40.625°$, α-$(Al_xGa_{1-x})_2O_3$ 0006 in the 2θ range of 40.625–41.67°, and α-Al_2O_3 0006 at $2\theta = 41.67°$, which shows that the α-Ga_2O_3 epitaxial films was successfully grown on the α-$(Al_xGa_{1-x})_2O_3$ layer without the inclusion of other phases. Under the high growth temperature, the inclusion of semi-stable ε-Ga_2O_3 and the thermodynamically stable phase β-Ga_2O_3 were detected at 2θ values of 39.81 and 38.20°, respectively (Supplementary Materials Fig. S2). Hao et al. reported a similar tendency with the temperature dependency of the crystal phase [36]. By increasing the number of α-$(Al_xGa_{1-x})_2O_3$ layers, in up to 3 layers of α-$(Al_xGa_{1-x})_2O_3$, the 0006 reflection of α-Ga_2O_3 can be identified. However, for the sample C with graded α-$(Al_xGa_{1-x})_2O_3$ layers, the XRD peaks merged in the 2θ range of 40.83–41.28°, which hindered the observation of α-$(Al_xGa_{1-x})_2O_3$ peaks. For the alloy composition, the $2\theta/\omega$ peak positions are affected by epitaxial strain caused by lattice mismatch. The peak positions of the strained epilayers were shifted, which caused an inaccurate alloy composition calculation [37]. To make an accurate estimate of the Al content in the α-$(Al_xGa_{1-x})_2O_3$ layers, energy-dispersive X-ray spectroscopy (EDS) analysis was conducted, as shown in Fig. 3a. X-ray rocking curves (XRC) were conducted to investigate the crystal quality of epitaxial α-Ga_2O_3/α-$(Al_xGa_{1-x})_2O_3$ grown on the sapphire substrate. The full width at half maximums (FWHMs) for α-Ga_2O_3 0006 and α-Ga_2O_3 $10\bar{1}4$ reflections for the sample A, B, and C were shown in Fig. 2d. The FWHMs value of the $10\bar{1}4$ peak decreased from 1913 to 1174 arcsec as the number of α-$(Al_xGa_{1-x})_2O_3$ layers increased from a single layer to a graded layer, which was reduced by 64.9% compared to directly grown on the sapphire substrate. Although the FWHMs value of the 0006 peak increased from 48 to 62.9 arcsec, this result was not significantly affected by the overall crystal quality of α-Ga_2O_3. Generally, the FWHMs value for α-Ga_2O_3 0006 and α-Ga_2O_3 $10\bar{1}4$ is correlated to screw and edge dislocation densities [24]. For heteroepitaxial α-Ga_2O_3/α-$(Al_xGa_{1-x})_2O_3$ grown on a sapphire substrate, the narrow FWHMs value for α-Ga_2O_3 0006 indicates better crystallinity compared to α-Ga_2O_3 $10\bar{1}4$ which means that the in-plane orientation of α-Ga_2O_3 grains were more twisted than the out-of-plane orientation of the α-Ga_2O_3 grains. Table 1 summarizes the crystal properties for samples A, B, and C in terms of Al content, in-plane lattice mismatch (%) of α-$(Al_xGa_{1-x})_2O_3$ with different configurations, and the FWHMs of α-Ga_2O_3 0006 and α-Ga_2O_3 $10\bar{1}4$.

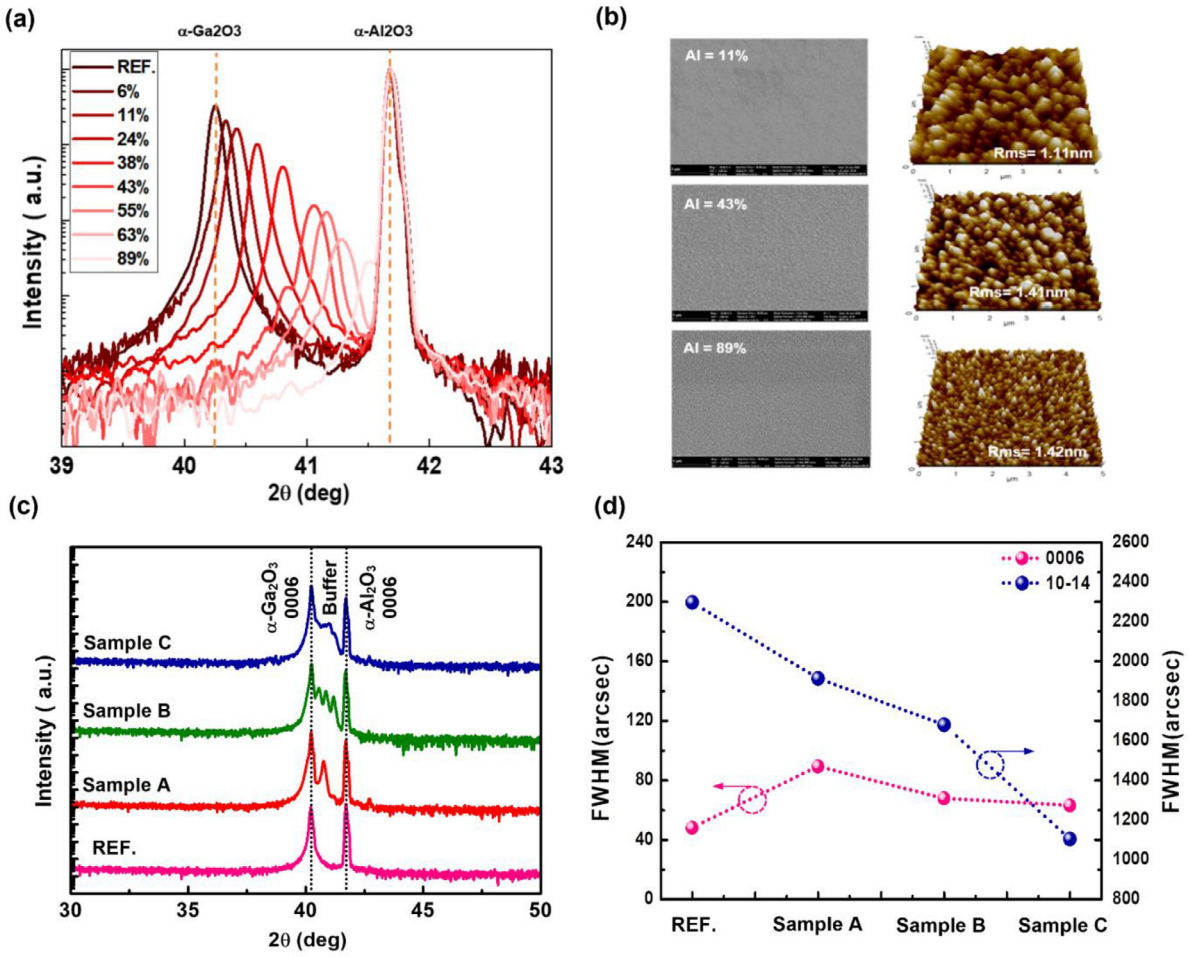

Fig. 2. (a) X-ray diffraction (XRD) $2\theta/\omega$ scan profiles for α-$(Al_xGa_{1-x})_2O_3$ with different Al content grown on a sapphire substrate. The vertical dotted lines represent the α-Ga_2O_3 0006 and α-Al_2O_3 0006 peak positions. (b) Plan-view FE-SEM images and the corresponding AFM images of α-$(Al_xGa_{1-x})_2O_3$ with different Al content. (c) XRD $2\theta/\omega$ spectra of samples grown on the different buffer layers. (d) High-resolution XRD ω-rocking scans for FWHMs of samples grown on different buffer layers for α-Ga_2O_3 0006 and $10\bar{1}4$ reflections.

Table 1
Summary of structure (buffer thickness, Al composition, lattice mismatch) and the FWHMs for the α-Ga_2O_3 0006 and $10\bar{1}4$ reflections.

	Buffer layer (0.35 μm)			**α-Ga_2O_3 layer (2 μm)**	
	Al composition(%)		In-plane misfit(%)	ω - rocking curve FWHMs(arcsec)	
				0006	$10\bar{1}4$
REF.	-	-	~ 4.6	48.06	2286.43
Sample A	1-layer	52	~ 2.4	89.31	1913.57
Sample B	3-layer	64,41,20	~ 0.92	67.72	1499.97
Sample C	Graded layer	82→60→52→24→11	~ 0.5	62.97	1174.28

Fig. 3 shows the cross-sectional scanning transmission electron microscopy (STEM) images of the sample structure and the elemental distribution of the α-$(Al_xGa_{1-x})_2O_3$ layer for the sample A, B, and C along with the $[0001]_{sapphire}$ direction. The STEM images in Fig. 3a, d, and g show a 0.35-μm-thick α-$(Al_xGa_{1-x})_2O_3$ layer with the different amounts of Al. The Al, Ga, and O atomic percent were represented by red, green, and olive lines. The decrease in the atomic percent of the red line indicated a decrease in Al content towards the growth direction, as shown in Fig. 3b, e, and h. Though the XRD peaks of the graded α-$(Al_xGa_{1-x})_2O_3$ layers were merged for the sample C, we confirmed the α-$(Al_xGa_{1-x})_2O_3$ graded buffer with an Al content of x = 11–82% through an EDS line profile analysis. In addition, the Al content measured from the EDS line in each layer for sample A and B was in good agreement with the Al content determined from the XRD peaks. Fig. 3c, f, and i show the images of EDS 2D mapping corresponding to the EDS line profile analysis, which also showed a consistent tendency of the elemental distribution of atomic percent of Al, Ga, and O in the α-$(Al_xGa_{1-x})_2O_3$ layers. In addition, magnified cross-sectional STEM images show the evolution of the growth mode change according to the density of islands in α-$(Al_xGa_{1-x})_2O_3$ based on the Al composition, as shown in Fig. 3b, e, and h. From the results in Fig. 2b and STEM analysis, it is expected that three-dimensional (3D) growth with a high density of islands was dominant during the growth of high Al content α-$(Al_xGa_{1-x})_2O_3$ since Al adatoms have lower migration than Ga adatoms on the sapphire substrate. In contrast, as the high Ga contents in the growth of α-$(Al_xGa_{1-x})_2O_3$ increased, a longer diffusion length of the Ga adatoms promoted lateral growth, which resulted in the larger grain size and two-dimensional (2D) growth with a low density of islands [33,34].

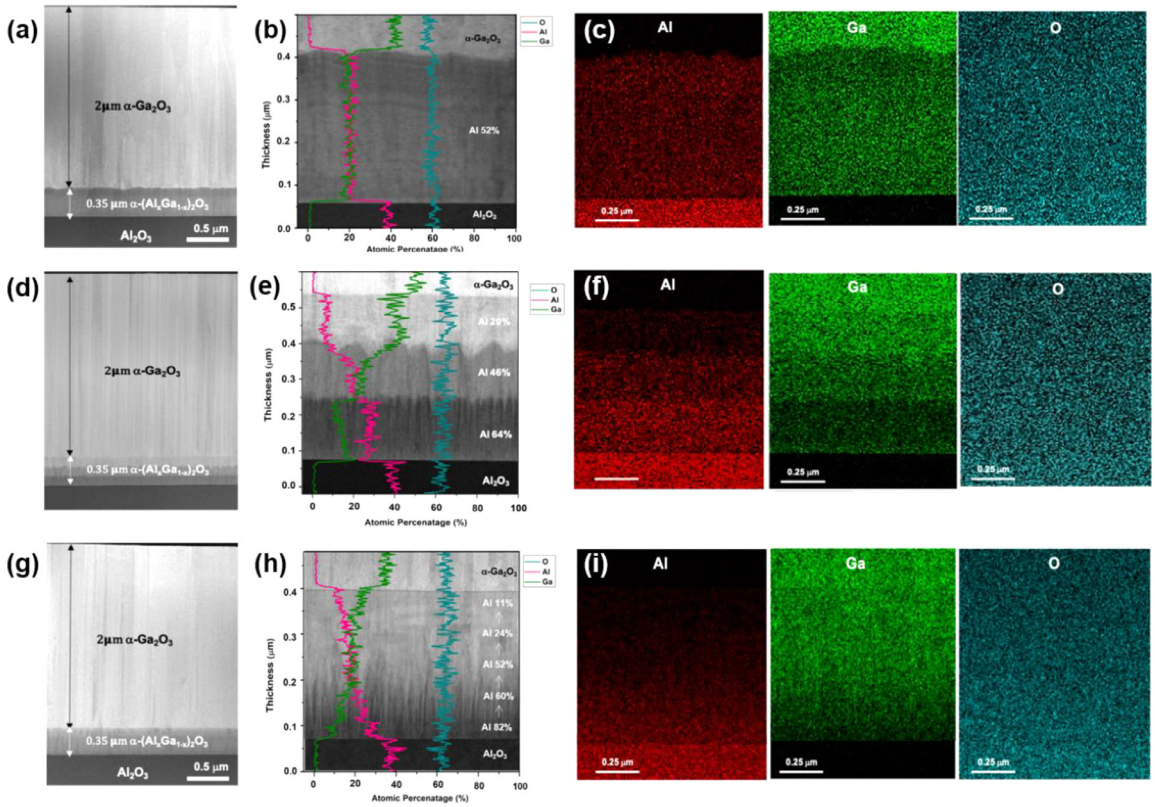

Fig. 3. Cross-sectional STEM images of the (a) sample A, (d) sample B, and (g) sample C. Energy-dispersive X-ray spectroscopy (EDS) elemental line profile of the (b) sample A, (e) sample B, and (h) sample C. The corresponding EDS mapping of elements (Al, Ga, and O) from the same area in STEM image of the (c) sample A, (f) sample B, and (i) sample C.

Therefore, the change of growth mode according to the density of islands in the α-$(Al_xGa_{1-x})_2O_3$ layer contributed to strain relaxation and dislocations propagation in the α-$(Al_xGa_{1-x})_2O_3$ layer.

For deeper investigation of the strain distribution in α-$(Al_xGa_{1-x})_2O_3$ for the samples A, B, and C, the reciprocal space mapping (RSM) analysis around the $10\bar{1}10$ reflections of the epitaxial α-Ga_2O_3/α-$(Al_xGa_{1-x})_2O_3$ grown on the sapphire substrates were conducted. Fig. 4a–c shows the RSM of the $10\bar{1}10$ reflections from samples A, B, and C, respectively. From RSM theory, the strain states in the α-$(Al_xGa_{1-x})_2O_3$ layers could be analyzed by the relative positions of the reciprocal lattice points (RLPs) of α-$(Al_xGa_{1-x})_2O_3$ peaks with respect to those of the underlying layers relative position [38]. For example, the reciprocal lattice points (RLPs) of the α-$(Al_xGa_{1-x})_2O_3$ peaks on a dashed orange or red line indicated that the corresponding lines were under fully relaxed or fully strained states with respect to the sapphire substrate, respectively. Fig. 4a shows the RLP of the α-$(Al_xGa_{1-x})_2O_3$ peaks were slightly above the orange dotted line, which means that the in-plane lattice constant of α-$(Al_xGa_{1-x})_2O_3$ was elongated by tensile forces. In contrast, for sample B and C, the RLP of α-$(Al_xGa_{1-x})_2O_3$ peaks close to sapphire substrate lay on the dashed orange line, which indicated that the α-$(Al_xGa_{1-x})_2O_3$ layer was in a fully relaxed state. In addition, the RLP of the subsequent α-$(Al_xGa_{1-x})_2O_3$ layer was positioned between the red and orange dashed line, which means that subsequent α-$(Al_xGa_{1-x})_2O_3$ layers were in a compressively strained state, as shown in Fig. 4b, c. This evolution of the RLPs indicated that the different configurations of α-$(Al_xGa_{1-x})_2O_3$ layer induced the compressive strain from the lattice mismatch significantly affected the strain distribution in the α-$(Al_xGa_{1-x})_2O_3$ layers.

Fig. 4d shows the evolution of the in-plane strain toward the growth direction as a function of Al content (x). Details of the calculation of the lattice parameter of α-Ga_2O_3 and α-$(Al_xGa_{1-x})_2O_3$ for all samples were provided in Table S1 (Supplementary Material). Based on the above analyses, the evolution of strain distribution in the α-$(Al_xGa_{1-x})_2O_3$ layer can be clarified. It is seen that the high Al content α-$(Al_xGa_{1-x})_2O_3$ islands have smaller in size and higher in density than those with low Al content owing to the shorter migration length of Al than that of Ga in initial growth. When the high density of α-$(Al_xGa_{1-x})_2O_3$ islands in initial growth on sapphire substrate, this high density of α-$(Al_xGa_{1-x})_2O_3$ islands introduced tensile strain at the coalescence boundaries to minimize the sum of elastic energy and surface energy. Therefore, the preserved compressive strain from the lattice mismatch was quickly relaxed by tensile strain in the initial growth on the sapphire substrate. As a result, all samples were under tensile strain in the vicinity of the epi/sub interface. Besides, the reported thermal expansion coefficient of α-Ga_2O_3 is larger than that of sapphire and, therefore, the tensile strain generated upon cooling down [39,40]. For the sample A without graded α-$(Al_xGa_{1-x})_2O_3$ layer, the thermal strain from the large thermal expansion coefficients were also under in Sample A. Therefore, the α-$(Al_xGa_{1-x})_2O_3$ layer for sample A was totally under tensile strain.

On the other hand, for the samples B and C with graded α-$(Al_xGa_{1-x})_2O_3$ layer, the increase of Ga content under growing graded α-$(Al_xGa_{1-x})_2O_3$ layer led to a decrease in density and a increase in the size of islands as shown in Fig. 3e, h. Furthermore, the lower density and larger size of islands induced the reduced tensile strain from island coalescence. Therefore, the relaxation of compressive strain can be reduced, and the more compressive strain can be built in graded α-$(Al_xGa_{1-x})_2O_3$ layer. In addition, the different thermal expansion coefficients were gradually reduced by the graded α-$(Al_xGa_{1-x})_2O_3$ layer, and thus lower thermal tensile strain could be built up in α-$(Al_xGa_{1-x})_2O_3$ layer.

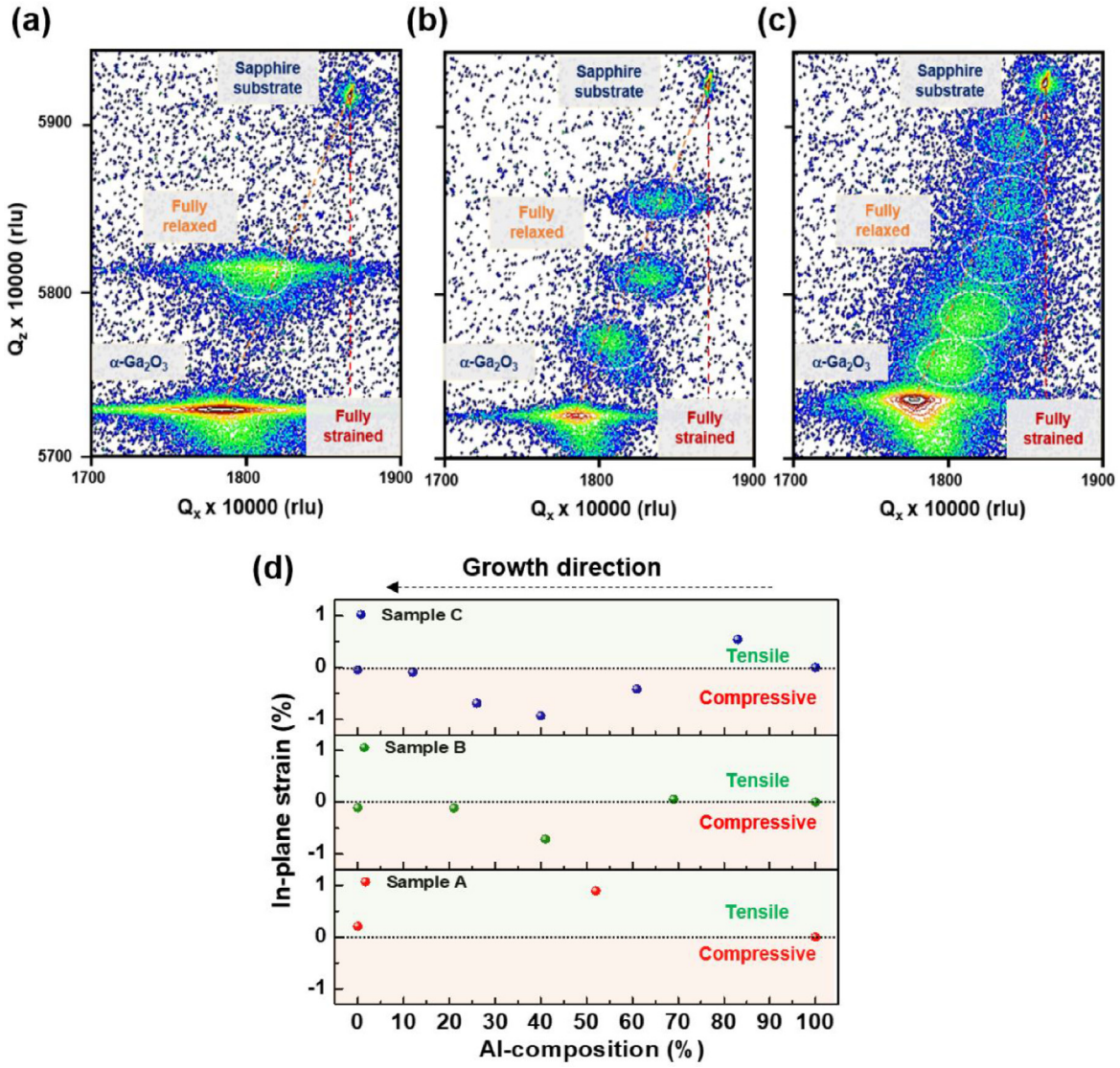

Fig. 4. Reciprocal space maps of the samples with different buffer configurations. Reciprocal space maps of the (a) sample A, (b) sample B, and (c) sample C around the $10\bar{1}10$. (d) the evolution of the in-plane strain (%) for α-Ga_2O_3/α-$(Al_xGa_{1-x})_2O_3$/sapphire substrate for the samples A, B, and C.

Hence, the preserved compressive strain can effectively compensate the thermal tensile strain and coalescence tensile strain in α-$(Al_xGa_{1-x})_2O_3$ layer. As a result, the sample C with a lower misfit between adjacent layers than that of the sample B has more reduced compressive strain relaxation and then, more compressive strain in the α-$(Al_xGa_{1-x})_2O_3$ layer.

We further investigated the mechanism of dislocations annihilation depending on the strain states. TEM analysis was conducted on the Sample A and Sample C with zone axis of $[11\bar{2}0]$. The TEM image for the samples A showed that the near-interface region of the α-$(Al_xGa_{1-x})_2O_3$/sapphire substrate had a huge defect with a high density of dislocations, and the TDs vertically propagated into the upper α-Ga_2O_3 layer without dislocation bending and annihilation, as shown in Fig. 5a. In contrast, for the sample C with graded α-$(Al_xGa_{1-x})_2O_3$ layer, the dislocations induced by the initial high density islands were inclined and interacted with each other. Based on the RSM analysis results as shown in Fig. 4d, the more preserved compressive strain in a graded α-$(Al_xGa_{1-x})_2O_3$ layer for sample C caused the inclination of dislocations and more dislocations annihilation, which resulted in high crystallinity of α-Ga_2O_3. Fig. 5b and e show the corresponding high-resolution TEM images of the near-interface region of α-Ga_2O_3/α-$(Al_{52}Ga_{48})_2O_3$ and α-$(Al_{52}Ga_{48})_2O_3$/sapphire. In addition, the images in Fig. 5c and 5f were acquired by selected fourier filtering of the corresponding rectangular area in Fig. 5b and 5e, respectively. Considering the high lattice mismatch between the α-Ga_2O_3/α-$(Al_{52}Ga_{48})_2O_3$/sapphire substrate for sample A, it was confirmed that a relatively high density of lattice distortions was generated near each interface. In contrast, the graded α-$(Al_xGa_{1-x})_2O_3$ layer with less than 0.56% lattice mismatch revealed fewer lattice distortions in the near-interface, as shown in Fig. 5j and m. Generally, the lattice mismatch for α-Ga_2O_3 directly grown on sapphire substrate induced the compressive strain at the α-Ga_2O_3/sapphire substrate on epitaxial growth. The misfit dislocations were generated when the compressive lattice strain was released at each interface, and then these interfacial misfit dislocations propagated upwards, resulting in the formation of threading dislocations. However, with a graded α-$(Al_xGa_{1-x})_2O_3$ layer for sample C, the reduced compressive lattice strain, which comes from the low lattice mismatch between adjacent layers, decreased the probability of formation of misfit dislocation, Moreover, benefiting from the number of the adjacent layer in graded

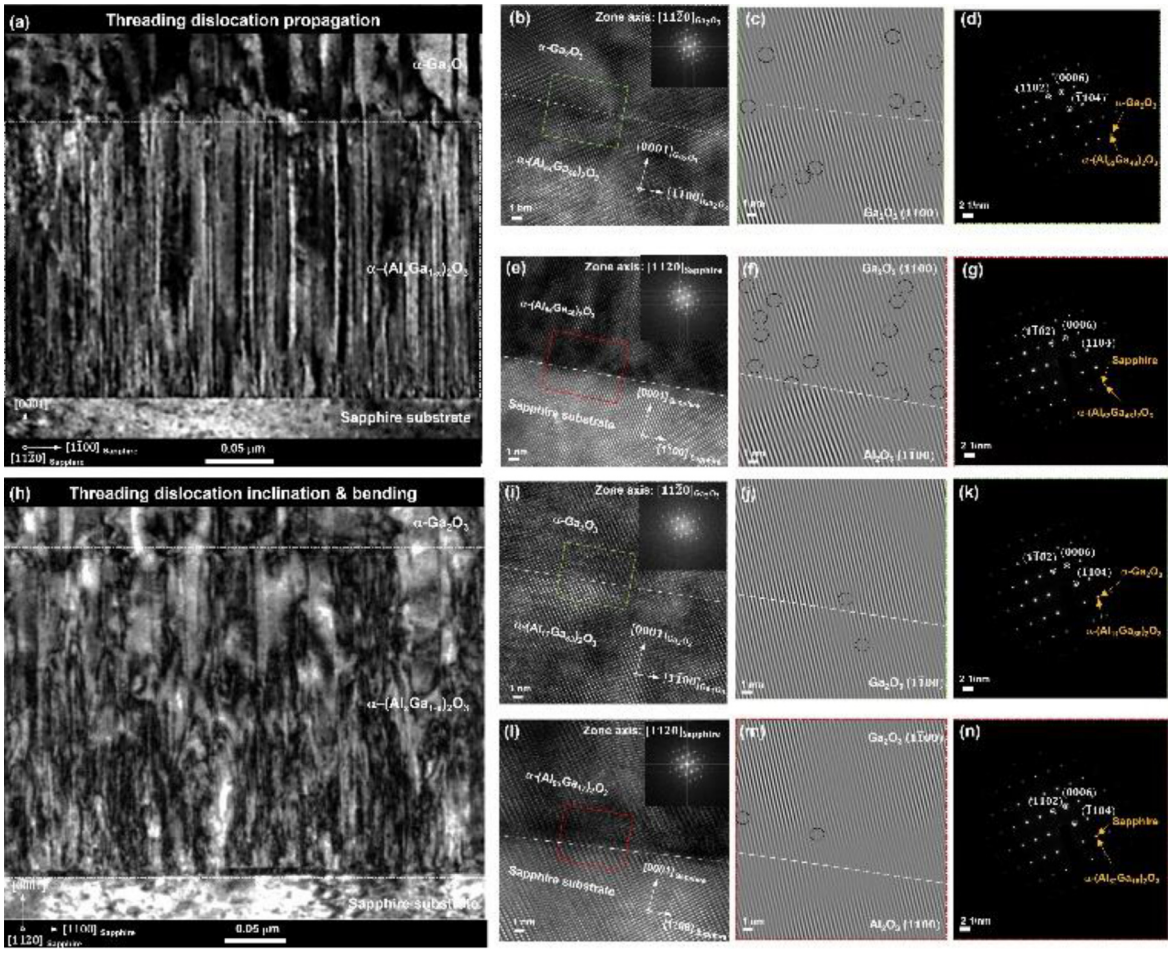

Fig. 5. Cross-section TEM images of (a) the sample A and (h) the sample C with zone axis [11$\bar{2}$0]. High-resolution TEM (HR-TEM) images and corresponding the fast fourier transforms (FFTs) in the inset for the sample A near the interfaces of (b) α-Ga_2O_3/α-$(Al_{52}Ga_{48})_2O_3$ and (e) α-$(Al_{52}Ga_{48})_2O_3$/sapphire and for the sample C near the interfaces of (i) α-Ga_2O_3/α-$(Al_{11}Ga_{89})_2O_3$ and (l) α-$(Al_{82}Ga_{18})_2O_3$/sapphire. (c), (f), (j), and (m) are the reconstructed TEM images at the rectangular region of the HR-TEM image. The circles highlights misfit dislocations near the interface. (d), (g), (k), and (n) are the corresponding selected area electron diffraction (SAED) patterns.

α-$(Al_xGa_{1-x})_2O_3$ layer, the generated interfacial misfit dislocations were bent at interface layer and thereby, lower threading dislocations were founded in graded α-$(Al_xGa_{1-x})_2O_3$ layer. Fig. 5d, g, k, and n show the selected area electron diffraction (SAED) patterns obtained from the interface of α-Ga_2O_3/α-$(Al_xGa_{1-x})_2O_3$ and α-$(Al_xGa_{1-x})_2O_3$/sapphire for the samples A and C, respectively. SAED patterns were acquired from both the sample A and C with zone axis [11$\bar{2}$0] show the anticipated corundum structure, which had the same crystal structure as the sapphire substrate.

Generally, the heteroepitaxial thin film is represented by a mosaic block, which assumed that it consisted of misoriented grains in the horizontal and vertical directions of the thin films. For α-Ga_2O_3 thin films, a mosaic model is an effective approach to quantitatively analyze tilt and twist angle, as shown in Fig. 6a [41]. The tilt and twist angle of the α-Ga_2O_3 thin films were extracted from the ω-scan of the symmetric and skew-symmetric reflections [42]. The tilt angle was extracted from the FWHMs of the out of the plane reflection of 0006. Broadening the FWHMs of the out-of-plane refection indicated the crystal quality in the normal direction of the thin films. On the other hand, the twist angle was extracted from the FWHMs of the measured ω-scan of 11$\bar{2}$6, 10$\bar{1}$10, 10$\bar{1}$4, 10$\bar{1}$2, and 11$\bar{2}$3 skew-symmetric reflections using the extrapolation method of the FWHMs proposed by Srikant et al [43]. The pseudo-voigt function was used for peak fitting, and the values obtained for tilt and twist angle are summarized in Table 2. Fig. 6b shows that with the insertion of the graded α-$(Al_xGa_{1-x})_2O_3$ layer, the α-Ga_2O_3 twist angle was reduced by 43.8% compared to without the graded α-$(Al_xGa_{1-x})_2O_3$ layer. Based on the calculated tilt (α_{tilt}), twist (α_{twist}) angle as shown in Fig.6 b, the screw (N_s) and edge (N_E) dislocation densities in α-Ga_2O_3 can be calculated the following two equations [43].

$$N_s = \frac{{\alpha_{tilt}}^2}{4.35b_s^2}$$

$$N_E = \frac{{\alpha_{twist}}^2}{4.35b_E^2}$$

Where N_s (N_E), α_{tilt} (α_{twist}), and b_s(b_E) indicate the screw, edge dislocation density, the tilt, twist angle, and length of burgers vector for screw, edge type dislocation components, respectively. From the burgers vectors $b_S = \langle 0001 \rangle$ and $b_E = \frac{1}{3}\langle 2\bar{1}\bar{1}0 \rangle$, the edge and screw dislocations of α-Ga_2O_3 for all samples were calculated in Table 2. In the case of sample C, the edge-dislocations density was reduced by 64.9% compared to the α-Ga_2O_3 directly grown on the bare sapphire substrate. This reduction of edge-dislocation revealed that the efficient compressive strain caused dislocations to incline in the graded α-$(Al_xGa_{1-x})_2O_3$ layer, and these inclined threading dislocations were encountered and annihilated with others. In subsequent α-Ga_2O_3 growth, with fewer misorientations of α-Ga_2O_3 on the α-$(Al_xGa_{1-x})_2O_3$ layer, the edge dislocations density of α-Ga_2O_3 decreased clearly by 64.9% compared to the α-Ga_2O_3 without graded α-$(Al_xGa_{1-x})_2O_3$ layer.

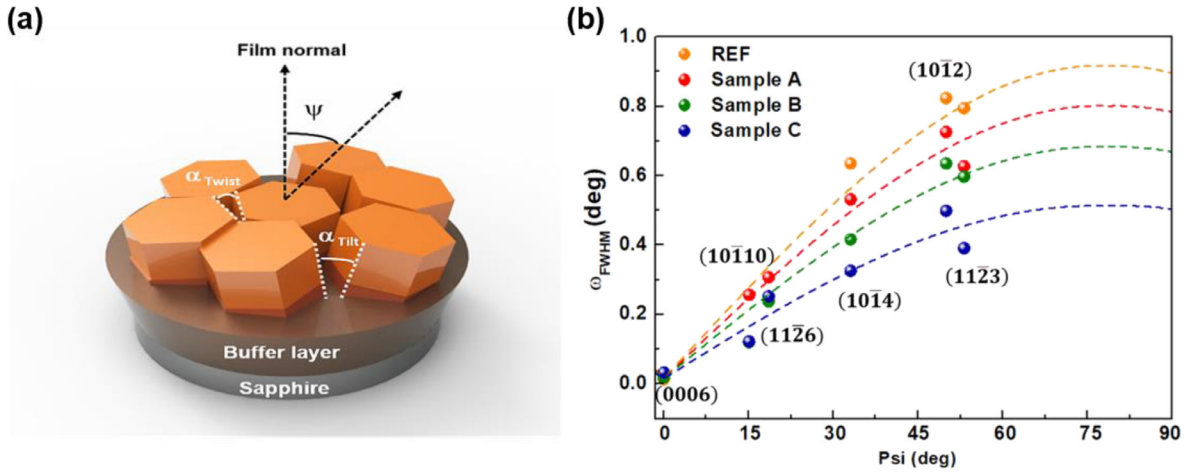

Fig. 6. (a) Schematic X-ray diffraction (XRD) measurement model for the tilt and twist structure. (b) FWHMs (ω) as a function of inclination angle. The points represent the experimental data, and the lines represent the fittings by the Srikant model [43].

Table 2
Summary of crystalline distortion tilt and twist angles and corresponding dislocation density for REF. and the sample A, B, and C.

	Crystalline distortion				Dislocation density	
	α tilt		α twist		Screw-dislocation density(cm^{-2})	Edge-dislocation density(cm^{-2})
	(degree)	(arcsec)	(degree)	(arcsec)		
REF.	0.013	46.8	0.896	3225.6	1.91×10^{6}	2.08×10^{10}
Sample A	0.024	86.4	0.783	2818.8	3.54×10^{6}	1.13×10^{10}
Sample B	0.018	64.8	0.669	2408.4	2.69×10^{6}	9.68×10^{9}
Sample C	0.032	113.5	0.503	1810.8	4.68×10^{6}	7.29×10^{9}

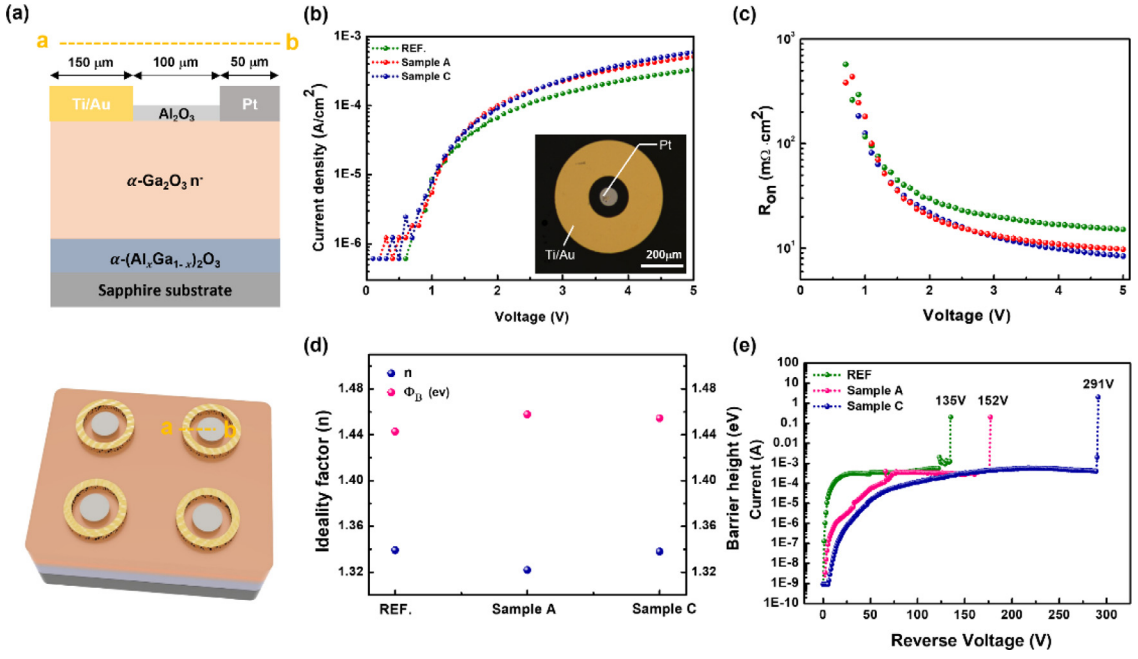

Fig. 7. (a) Schematic of the α-Ga_2O_3 Schottky diodes. (b) Log-scale measured forward *J-V* characteristics. The optical microscopy image of the Schottky diodes is shown in the inset. (c) Log-scale measured R_{on}-*V* characteristics. (d) The ideality factor and Schottky barrier height of the α-Ga_2O_3 Schottky diodes. (e) The log-scale measured reverse *I-V* characteristics.

The effect of threading dislocations reduction on α-Ga_2O_3 electrical properties remains elusive. To investigate the correlation between TDs and device performance, 2.0-μm-thick n^- α-Ga_2O_3 layers were grown on a single α-$(Al_xGa_{1-x})_2O_3$ layer and a graded α-$(Al_xGa_{1-x})_2O_3$ layer. The 2.0-μm-thick n^- α-Ga_2O_3 on sapphire showed an electron concentration (n) was 4.397×10^{18} cm^{-3} and Hall mobility (μ) of 0.78 $cm^2/V{\cdot}s$. Fig. 7a presents the schematic of the α-Ga_2O_3 Schottky diodes with an α-$(Al_xGa_{1-x})_2O_3$ layer, and the corresponding $2\theta/\omega$ scan was presented in Fig. S3a. The FWHMs value of α-Ga_2O_3 0006 and α-Ga_2O_3 10$\bar{1}$4 were summarized in Table 3. The FWHMs value of the 0006 diffraction was estimated to be about 60~66 arcsecs. On the other hand, the FWHMs value of the 10$\bar{1}$4 diffraction for the sample A and B were smaller than that of the undoped α-Ga_2O_3, which indicated that the Sn

Table 3
Summary of properties of the α-Ga_2O_3 Schottky diodes.

	ω - rocking curve FWHM(arcsec)		Ideality factor(n)	Barrier height(eV)	R_{on}(mΩcm^2)	BreakdownVoltage(V)	Figure of meritV_{BR}^2/ R_{on} (MW/cm^2)
	0006	$10\bar{1}4$					
REF.	61.45	1391.59	1.34	1.44	15.11	135	1.21
Sample A	66.58	961.48	1.32	1.46	9.74	152	2.37
Sample C	60.31	850.76	1.33	1.45	8.40	291	10.1

doping could reduce the threading dislocations density and led to improvement in the crystallinity [44,45].

Fig. 7b, c shows the forward *J-V* and the differential specific on-resistance R_{on} (dV/dI) characteristics of the α-Ga_2O_3 Schottky diodes in log scale. The extracted R_{on} of the samples A, B, and C is estimated to be 15.11, 9.74, and 9.40 m$\Omega\cdot$cm^2, respectively. The difference in R_{on} suggests that the electron-defect scattering was reduced due to low defect density in the α-$(Al_xGa_{1-x})_2O_3$ layer, which resulted in increasing conductance of the drift layer. Under the condition that V >> 3KT/q, the general diode equation by the thermal emission (TE) model is given by [46]

$$I = I_0\left[exp\left(\frac{qv}{nkT}\right) - 1\right]$$

where I_0 is the saturation current. I_0 is given by

$$I_0 = AA^{**}T^2exp\left[-\frac{q\emptyset_B}{nkT}\right]$$

where A is the Schottky contact area, and A** is the Richardson constant (40.8 A$\cdot$cm^{-2}) [47]. The ideality factor and the saturation current can be obtained from the slope and the intercept of the log *J-V* plot, respectively. Fig. 7d shows the crystal quality dependence of the ideality factor and barrier height, indicating that barrier height inhomogeneity led to the deviation of the *J-V* characteristics from the TE model [48]. The reverse breakdown characteristics for the α-Ga_2O_3 Schottky diodes were shown in Fig. 7e. The breakdown voltage for the three samples were estimated to be 135 V, 152 V, and 291 V, respectively. From the reverse *I-V* characteristics, it is found that the breakdown voltage (V_{BR}) of the α-Ga_2O_3 Schottky diodes with low TDD was higher than those with high TDD. The difference in V_{BR} revealed that with the graded α-$(Al_xGa_{1-x})_2O_3$ layer, the leakage current paths caused by threading dislocations paths were reduced, which resulted in a higher V_{BR} and consequently preferable high voltage power devices. The figure of merit of V_{BR}^2/R_{on} for the α-$(Al_xGa_{1-x})_2O_3$ Schottky diodes with the graded α-$(Al_xGa_{1-x})_2O_3$ layer was 10.1 MW/cm^2, almost 5 times higher than the V_{BR}^2/R_{on} value of 2.37 MW/cm^2 for the Schottky diodes with single α-$(Al_xGa_{1-x})_2O_3$ layer as shown in Table 3. Therefore, the graded α-$(Al_xGa_{1-x})_2O_3$ layer can contribute to better crystal quality with low dislocation density, which results in a higher V_{BR} and a greater current density.

4. Conclusion

We demonstrated high-quality α-Ga_2O_3 epitaxial films by adopting a graded α-$(Al_xGa_{1-x})_2O_3$ buffer layer with x = 0.11–0.87, which resulted in an observable reduction of threading dislocations density compared to a single α-$(Al_xGa_{1-x})_2O_3$ buffer layer. Based on RSM strain and TEM analyses, the mechanism of strain relaxation and dislocation annihilation using the graded α-$(Al_xGa_{1-x})_2O_3$ layer can be clarified. The preserved greater compressive strain caused to dislocations to incline in the graded α-$(Al_xGa_{1-x})_2O_3$ layer, and these inclined threading dislocations were encountered and annihilated with others. Moreover, owing to the annihilated threading dislocations, the 2.0-μm-thick α-Ga_2O_3 layer on a α-$(Al_xGa_{1-x})_2O_3$ layer had fewer twist misorientation grains, which was reduced by 43.8% compared to those without a graded α-$(Al_xGa_{1-x})_2O_3$ layer. To investigate the effect of dislocation reduction on performance of α-Ga_2O_3 Schottky diodes, 2.0-μm-thick n$^-$ α-Ga_2O_3 layers were grown on a single α-$(Al_xGa_{1-x})_2O_3$ layer and the graded α-$(Al_xGa_{1-x})_2O_3$ layer. The α-Ga_2O_3 Schottky diodes with the graded α-$(Al_xGa_{1-x})_2O_3$ layer showed the lower on-resistance (R_{on}) of 8.40 m$\Omega\cdot$cm^2, the higher breakdown voltage (V_{BR}) of 291 V, and the higher figure of merit (V_{BR}^2/R_{on}) of 10.1 MW/cm^2 than that without the graded α-$(Al_xGa_{1-x})_2O_3$ layer, respectively. In this way, the strain relaxation and dislocation annihilation in the graded α-$(Al_xGa_{1-x})_2O_3$ layer contributed to better crystal quality with low dislocation density in α-Ga_2O_3, consequently resulted in a higher V_{BR} and a greater current density. This study can provide an attractive approach for obtaining high-quality epitaxial α-Ga_2O_3 thin films for high voltage power devices.

Declaration of Competing Interest

The authors declare that they have no known competing financial interests or personal relationships that could have appeared to influence the work reported in this paper.

Acknowledgments

This research was supported by the Strategic Core Material Development Program through the Korea Evaluation Institute of Industrial Technology (KEIT) funded by the Ministry of Trade, Industry, and Energy (MOTIE) (no. 10080736). The Inter-University Semiconductor Research Center and Institute of Engineering Research at Seoul National University provided research facilities for this work. The Innovative Process Design Center for Strategic Structural Materials (2020R1A5A6017701) through the Engineering Research Center

Supplementary materials

Supplementary material associated with this article can be found, in the online version, at doi:10.1016/j.actamat.2021.117423.

References

[1] S.B. Reese, T. Remo, J. Green, A. Zakutayev, How much will gallium oxide power electronics cost? Joule 3 (2019) 903–907, doi:10.1016/j.joule.2019.01.011.
[2] X. Ding, J. Cheng, F. Chen, Impact of silicon carbide devices on the powertrain systems in electric vehicles, Energies 10 (2017) 1–17, doi:10.3390/en10040533.
[3] J.Y. Tsao, S. Chowdhury, M.A. Hollis, D. Jena, N.M. Johnson, K.A. Jones, R.J. Kaplar, S. Rajan, C.G. Van de Walle, E. Bellotti, C.L. Chua, R. Collazo, M.E. Coltrin, J.A. Cooper, K.R. Evans, S. Graham, T.A. Grotjohn, E.R. Heller, M. Higashiwaki, M.S. Islam, P.W. Juodawlkis, M.A. Khan, A.D. Koehler, J.H. Leach, U.K. Mishra, R.J. Nemanich, R.C.N. Pilawa-Podgurski, J.B. Shealy, Z. Sitar, M.J. Tadjer, A.F. Witulski, M. Wraback, J.A. Simmons, Ultrawide-bandgap semiconductors: research opportunities and challenges, Adv. Electron. Mater. 4 (2018), doi:10.1002/aelm.201600501.
[4] W.S. Hwang, A. Verma, H. Peelaers, V. Protasenko, S. Rouvimov, H. Xing, A. Seabaugh, W. Haensch, C. Van De Walle, Z. Galazka, M. Albrecht, R. Fornari, D. Jena, High-voltage field effect transistors with wide-bandgap β -Ga $_2O_3$ nanomembranes, Appl. Phys. Lett. 104 (2014) 3–8, doi:10.1063/1.4879800.
[5] Y. Zhang, A. Neal, Z. Xia, C. Joishi, J.M. Johnson, Y. Zheng, S. Bajaj, M. Brenner, D. Dorsey, K. Chabak, G. Jessen, J. Hwang, S. Mou, J.P. Heremans, S. Rajan, Demonstration of high mobility and quantum transport in modulation-doped β-(AlxGa1-x$_2O_3$/Ga_2O_3 heterostructures, Appl. Phys. Lett. 112 (2018) 1–6, doi:10.1063/1.5025704.

[6] M.H. Wong, K. Sasaki, A. Kuramata, S. Yamakoshi, M. Higashiwaki, Electron channel mobility in silicon-doped Ga_2O_3 MOSFETs with a resistive buffer layer, Jpn. J. Appl. Phys. (2016) 55, doi:10.7567/JJAP.55.1202B9.

[7] S.I. Stepanov, V.I. Nikolaev, V.E. Bougrov, A.E. Romanov, Gallium oxide: properties and applications - a review, Rev. Adv. Mater. Sci. 44 (2016) 63–86.

[8] M. Higashiwaki, G.H. Jessen, Guest editorial: the dawn of gallium oxide microelectronics, Appl. Phys. Lett. 112 (2018), doi:10.1063/1.5017845.

[9] S. Nakagomi, T. Momo, S. Takahashi, Y. Kokubun, Deep ultraviolet photodiodes based on β-Ga_2O_3/SiC heterojunction, Appl. Phys. Lett. 103 (2013) 3–7, doi:10.1063/1.4818620.

[10] M.A. Mastro, A. Kuramata, J. Calkins, J. Kim, F. Ren, S.J. Pearton, Perspective – opportunities and future directions for Ga_2O_3, ECS J. Solid State Sci. Technol. 6 (2017) P356–P359, doi:10.1149/2.0031707jss.

[11] X.Z. Liu, P. Guo, T. Sheng, L.X. Qian, W.L. Zhang, Y.R. Li, β-Ga2O3 thin films on sapphire pre-seeded by homo-self-templated buffer layer for solar-blind UV photodetector, Opt. Mater. (Amst). 51 (2016) 203–207, doi:10.1016/j.optmat.2015.11.023.

[12] M. Higashiwaki, A. Kuramata, H. Murakami, Y. Kumagai, State-of-the-art technologies of gallium oxide power devices, J. Phys. D. Appl. Phys. (2017) 50, doi:10.1088/1361-6463/aa7aff.

[13] M. Bosi, P. Mazzolini, L. Seravalli, R. Fornari, Ga_2O_3polymorphs: Tailoring the epitaxial growth conditions, J. Mater. Chem. C 8 (2020) 10975–10992, doi:10.1039/d0tc02743j.

[14] H. Sun, K.H. Li, C.G.T. Castanedo, S. Okur, G.S. Tompa, T. Salagaj, S. Lopatin, A. Genovese, X. Li, HCl Flow-induced phase change of α-, β-, and ϵ-Ga_2O_3films grown by MOCVD, Cryst. Growth Des. 18 (2018) 2370–2376, doi:10.1021/acs.cgd.7b01791.

[15] R. Roy, V.G. Hill, E.F. Osborn, Polymorphism of Ga_2O_3 and the system Ga_2O_3 – H_2O, J. Am. Chem. Soc 74 (1952) 719–722 http://pubs.acs.org/doi/pdf/10.1021/ja01123a039%0Apapers2://publication/uuid/719181C7-468D-4F83-A316-AAAA010D31C5.

[16] H. Hayashi, R. Huang, F. Oba, T. Hirayama, I. Tanaka, Epitaxial growth of Mn-doped γ-Ga_2O_3 on spinel substrate, J. Mater. Res. 26 (2011) 578–583, doi:10.1557/jmr.2010.32.

[17] H. Aida, K. Nishiguchi, H. Takeda, N. Aota, K. Sunakawa, Y. Yaguchi, Growth of β-Ga_2O_3 single crystals by the edge-defined, film fed growth method, Jpn. J. Appl. Phys. 47 (2008) 8506–8509, doi:10.1143/JJAP.47.8506.

[18] Z. Galazka, R. Uecker, D. Klimm, K. Irmscher, M. Naumann, M. Pietsch, A. Kwasniewski, R. Bertram, S. Ganschow, M. Bickermann, Scaling-up of bulk β-Ga_2O_3 single crystals by the czochralski method, ECS J. Solid State Sci. Technol. 6 (2017) Q3007–Q3011, doi:10.1149/2.0021702jss.

[19] E. Ahmadi, Y. Oshima, Materials issues and devices of α- And β-Ga_2O_3, J. Appl. Phys. (2019) 126, doi:10.1063/1.5123213.

[20] S. Kan, S. Takemoto, K. Kaneko, I. Takahashi, M. Sugimoto, T. Shinohe, S. Fujita, Electrical properties of α-Ir_2O_3/α-Ga_2O_3 pn heterojunction diode and band alignment of the heterostructure, Appl. Phys. Lett. 113 (2018) 212104, doi:10.1063/1.5054054.

[21] M.T. Ha, K.H. Kim, Y.J. Shin, S.M. Jeong, S.Y. Bae, Leidenfrost motion of water microdroplets on surface substrate: epitaxy of gallium oxide via mist chemical vapor deposition, Adv. Mater. Interfaces 8 (2021) 1–8, doi:10.1002/admi.202001895.

[22] D. Shinohara, S. Fujita, Heteroepitaxy of corundum-structured α-Ga_2O_3 thin films on α-Al_2O_3 substrates by ultrasonic mist chemical vapor deposition, Jpn. J. Appl. Phys. 47 (2008) 7311–7313, doi:10.1143/JJAP.47.7311.

[23] K. Kawara, Y. Oshima, M. Okigawa, T. Shinohe, Elimination of threading dislocations in α-$Ga_2O_3$by double-layered epitaxial lateral overgrowth, Appl. Phys. Express. 13 (2020), doi:10.35848/1882-0786/ab9fc5.

[24] H. Son, Y.J. Choi, J.S. Ha, S.H. Jung, D.W. Jeon, Crystal quality improvement of α-Ga_2O_3 growth on stripe patterned template via epitaxial lateral overgrowth, Cryst. Growth Des. 19 (2019) 5105–5110, doi:10.1021/acs.cgd.9b00454.

[25] Y. Oshima, K. Kawara, T. Shinohe, T. Hitora, M. Kasu, S. Fujita, Epitaxial lateral overgrowth of α-Ga2O3 by halide vapor phase epitaxy, APL Mater 7 (2019) https://doi.org/10.1063/1.5051058.

[26] Y. Xu, J.H. Park, Z. Yao, C. Wolverton, M. Razeghi, J. Wu, V.P. Dravid, Strain-induced metastable phase stabilization in Ga_2O_3 thin films, ACS Appl. Mater. Interfaces 11 (2019) 5536–5543, doi:10.1021/acsami.8b17731.

[27] L.M. Giovane, H.C. Luan, A.M. Agarwal, L.C. Kimerling, Correlation between leakage current density and threading dislocation density in SiGe p-i-n diodes grown on relaxed graded buffer layers, Appl. Phys. Lett. 78 (2001) 541–543, doi:10.1063/1.1341230.

[28] M. Oda, K. Kaneko, S. Fujita, T. Hitora, Crack-free thick (>5 μm) a-Ga_2O_3 films on sapphire substrates with a-$(Al,Ga)_2O_3$ buffer layers, Jpn. J. Appl. Phys. 55 (2016) 1202B4, doi:10.7567/JJAP.55.1202B4.

[29] R. Jinno, T. Uchida, K. Kaneko, S. Fujita, Reduction in edge dislocation density in corundum-structured ?-Ga_2O_3 layers on sapphire substrates with quasi-graded ?-$(Al,Ga)_2O_3$ buffer layers, Appl. Phys. Express. 9 (2016), doi:10.7567/APEX.9.071101.

[30] G.T. Dang, S. Sato, Y. Tagashira, T. Yasuoka, L. Liu, T. Kawaharamura, α -$(AlxGa1-x)_2O_3$single-layer and heterostructure buffers for the growth of conductive Sn-doped α -Ga_2O_3thin films via mist chemical vapor deposition, APL Mater. 8 (2020), doi:10.1063/5.0023041.

[31] K. Kaneko, T. Nomura, S. Fujita, Corundum-structured α-phase Ga_2O_3-Cr_2O_3-Fe_2O_3 alloy system for novel functions, Phys. Status Solidi Curr. Top. Solid State Phys. 7 (2010) 2467–2470, doi:10.1002/pssc.200983896.

[32] H. Peelaers, J.B. Varley, J.S. Speck, C.G. Van De Walle, Structural and electronic properties of Ga_2O_3-Al_2O_3 alloys, Appl. Phys. Lett. 112 (2018), doi:10.1063/1.5036991.

[33] T. Uchida, K. Kusakabe, K. Ohkawa, Influence of polymer formation on metalorganic vapor-phase epitaxial growth of AlN, J. Cryst. Growth. 304 (2007) 133–140, doi:10.1016/j.jcrysgro.2007.01.022.

[34] S. Fung, X. Xiaoliang, Z. Youwen, S. Wenhong, C. Xudong, S. Niefung, S. Tongnian, J. Chunxiang, Gallium/aluminum interdiffusion between n-GaN and sapphire, J. Appl. Phys. 84 (1998) 2355–2357, doi:10.1063/1.368362.

[35] W.D. Nix, Surface roughening of, Mater. Sci. (1999) 173–209.

[36] J.G. Hao, T.C. Ma, X.H. Chen, Y. Kuang, L. Li, J. Li, F.F. Ren, S.L. Gu, H.H. Tan, C. Jagadish, J.D. Ye, Phase tailoring and wafer-scale uniform hetero-epitaxy of metastable-phased corundum α-Ga_2O_3 on sapphire, Appl. Surf. Sci. (2020) 513, doi:10.1016/j.apsusc.2020.145871.

[37] J. Perozek, H.P. Lee, B. Krishnan, A. Paranjpe, K.B. Reuter, D.K. Sadana, C. Bayram, Investigation of structural, optical, and electrical characteristics of an AlGaN/GaN high electron mobility transistor structure across a 200 mm Si(111) substrate, J. Phys. D. Appl. Phys. (2017) 50, doi:10.1088/1361-6463/aa5208.

[38] T. Roesener, V. Klinger, C. Weuffen, D. Lackner, F. Dimroth, Determination of heteroepitaxial layer relaxation at growth temperature from room temperature X-ray reciprocal space maps, J. Cryst. Growth. 368 (2013) 21–28, doi:10.1016/j.jcrysgro.2013.01.007.

[39] W.M. Yim, R.J. Paff, Thermal expansion of AlN, sapphire, and silicon, J. Appl. Phys. 45 (1974) 1456–1457, doi:10.1063/1.1663432.

[40] L.J. Eckert, R.C. Bradt, Thermal Expansion of Alpha Ga_2O_3, J. Am. Ceram. Soc. 56 (1973) 229–230, doi:10.1111/j.1151-2916.1973.tb12471.x.

[41] H.V. Stanchu, A.V. Kuchuk, P.M. Lytvyn, Y.I. Mazur, M.E. Ware, Y. Maidaniuk, M. Benamara, Z.M. Wang, G.J. Salamo, Kinetically controlled transition from 2D nanostructured films to 3D multifaceted InN nanocrystals on GaN(0001), CrystEngComm 20 (2018) 1499–1508, doi:10.1039/c7ce02070h.

[42] T.C. Ma, X.H. Chen, Y. Kuang, L. Li, J. Li, F. Kremer, F.F. Ren, S.L. Gu, R. Zhang, Y.D. Zheng, H.H. Tan, C. Jagadish, J.D. Ye, On the origin of dislocation generation and annihilation in α -Ga_2O_3 epilayers on sapphire, Appl. Phys. Lett. 115 (2019), doi:10.1063/1.5120554.

[43] V. Srikant, J.S. Speck, D.R. Clarke, Mosaic structure in epitaxial thin films having large lattice mismatch, J. Appl. Phys. 82 (1997) 4286–4295, doi:10.1063/1.366235.

[44] K. Akaiwa, K. Kaneko, K. Ichino, S. Fujita, Conductivity control of Sn-doped a-Ga_2O_3 thin films grown on sapphire substrates, Jpn. J. Appl. Phys. (2016) 55, doi:10.7567/JJAP.55.1202BA.

[45] K. Akaiwa, K. Ota, T. Sekiyama, T. Abe, T. Shinohe, K. Ichino, Electrical properties of Sn-Doped α-Ga_2O_3 films on m-plane sapphire substrates grown by mist chemical vapor deposition, Phys. Status Solidi Appl. Mater. Sci. 217 (2020) 1–5, doi:10.1002/pssa.201900632.

[46] D. Splith, S. Müller, F. Schmidt, H. Von Wenckstern, J.J. Van Rensburg, W.E. Meyer, M. Grundmann, Determination of the mean and the homogeneous barrier height of Cu Schottky contacts on heteroepitaxial β-Ga_2O_3 thin films grown by pulsed laser deposition, Phys. Status Solidi Appl. Mater. Sci. 211 (2014) 40–47, doi:10.1002/pssa.201330088.

[47] H. He, R. Orlando, M.A. Blanco, R. Pandey, E. Amzallag, I. Baraille, M. Rérat, First-principles study of the structural, electronic, and optical properties of Ga_2O_3 in its monoclinic and hexagonal phases, Phys. Rev. B Condens. Matter Mater. Phys. 74 (2006) 1–8, doi:10.1103/PhysRevB.74.195123.

[48] S. Kim, T.H. Seo, M.J. Kim, K.M. Song, E.K. Suh, H. Kim, Graphene-GaN Schottky diodes, Nano Res. 8 (2015) 1327–1338, doi:10.1007/s12274-014-0624-7.

[49] Byun Dong–Wook, Morphological and Electrical Properties of β–Ga 2 O 3 /4H–SiC Heterojunction Diodes, Electronic Materials Letters 17 (2021) 479–484, doi:10.1007/s13391-021-00297-6.

[50] Ha Minh-Tan, Effect of Hot-zone Aperture on the Growth Behavior of SiC Single Crystal Produced via Top-seeded Solution Growth Method, Journal of the Korean Ceramic Society 56 (2019) 589–595, doi:10.4191/kcers.2019.56.6.07.